NASA MEMO 5-20-59L

N-05
3M 2.20

NASA

MEMORANDUM

LOW-SUBSONIC MEASUREMENTS OF THE STATIC AND OSCILLATORY LATERAL STABILITY DERIVATIVES OF A SWEPTBACK-WING AIRPLANE CONFIGURATION AT ANGLES OF ATTACK FROM -10° TO 90°

By Donald E. Hewes

Langley Research Center
Langley Field, Va.

NATIONAL AERONAUTICS AND
SPACE ADMINISTRATION
WASHINGTON
June 1959

NATIONAL AERONAUTICS AND SPACE ADMINISTRATION

MEMORANDUM 5-20-59L

LOW-SUBSONIC MEASUREMENTS OF THE STATIC AND OSCILLATORY LATERAL STABILITY DERIVATIVES OF A SWEPTBACK-WING AIRPLANE CONFIGURATION AT ANGLES OF ATTACK FROM -10° TO 90°

By Donald E. Hewes

SUMMARY

An investigation has been conducted in the Langley free-flight tunnel at low-subsonic speeds to provide some basic information on the stability and control characteristics in the high angle-of-attack range of an airplane configuration typical of current design trends. The investigation consisted of static- and dynamic-force tests over an angle-of-attack range from -10° to 90°. The dynamic-force tests, which consisted of both linear- and rotary-oscillation tests, were conducted at values of the reduced-frequency parameter k of 0.10, 0.15, and 0.20. The configuration was directionally unstable for all angles of attack above about 15° but maintained positive effective dihedral, control effectiveness, and damping in roll and yaw over most of the angle-of-attack range tested. The effects of frequency on the oscillatory stability derivatives were found to be generally small, but in a few cases the effects were relatively large.

INTRODUCTION

Recent trends in airplane design have created a need for information on the stability and control characteristics of complete airplane configurations over a much larger range of angles of attack than that normally covered in most wind-tunnel investigations. One particular application where stability and control data for a very large range of angle of attack are required is in the study of stability and control problems of vertical-take-off-and-landing airplanes in hovering and transition flight. Another application is in the study of uncontrollable stalling and spinning maneuvers which have been encountered with current high-speed airplanes. The present investigation was undertaken to provide some basic information in the high-angle-of-attack range on the static and oscillatory lateral stability derivatives and control-effectiveness parameters for a sweptback-wing airplane configuration typical of current design trends. Somewhat similar investigations of a delta-wing and an unswept-wing configuration are reported in references 1 and 2, respectively.

The investigation consisted of static- and dynamic-force tests of a model of the swept-wing airplane configuration both with and without the vertical tail. Static-force tests were made to determine the static longitudinal and lateral stability of the configuration and the control effectiveness of the ailerons, rudder, and all-movable horizontal tail. In the dynamic-force tests the model was forced to oscillate at constant amplitude in roll, yaw, or sideslip relative to the body axes. In the case of the rotary-oscillation tests where the rotary motion about the body axis generated not only rolling and yawing velocities but also sideslipping velocities, the measurements consisted of combinations of the various lateral-stability derivatives. The tests were made at a Reynolds number of about 570,000 in the Langley free-flight tunnel and covered an angle-of-attack range from -10° to 90° and a range of the reduced-frequency parameter k from 0.10 to 0.20 for the dynamic tests.

DEFINITION OF TERMS AND SYMBOLS

All velocities, forces, and moments with the exception of lift and drag were measured with respect to the body-axis system originating at the reference center-of-gravity position located at 25.7 percent mean aerodynamic chord. (See fig. 1.) The term "in-phase derivative" used in this report refers to any one of the stability derivatives which are based on the forces or moments in phase with the angle of roll, yaw, or sideslip produced in the oscillatory tests. The term "out-of-phase derivative" refers to any one of the stability derivatives which are based on the forces or moments 90° out of phase with the angle of roll, yaw, or sideslip. All measurements are reduced to standard coefficient form and are presented in terms of the following symbols:

X,Y,Z	longitudinal, lateral, and normal body axes, respectively
X_s,Z_s	longitudinal and vertical stability axes, respectively
S	wing area, sq ft
b	wing span, ft
$\bar{c}$	mean aerodynamic chord, ft

c	chord
V	free-stream velocity, fps
q	free-stream dynamic pressure, lb/sq ft

$\omega = 2\pi f$ radian/sec

$k = \frac{\omega b}{2V}$

f	circular frequency, cps
y	lateral displacement, ft
α	angle of attack, deg
β	angle of sideslip, deg or radians
ψ	angle of yaw, deg or radians
ϕ	angle of roll, deg or radians
δ_a'	deflection of either aileron, positive with trailing edge down, deg
δ_a	differential aileron deflection, $\delta_{a,R}' - \delta_{a,L}'$, deg
δ_r	deflection of rudder, positive with trailing edge to left, deg
i_t	horizontal-tail incidence, positive with trailing edge down, deg
t	time, sec
I_X	moment of inertia about X-axis
I_Z	moment of inertia about Z-axis
r	yawing velocity, radian/sec
p	rolling velocity, radian/sec
F_L	lift, lb
F_D'	drag, lb

F_Y	side force, lb
M_{Y_S}	pitching moment, ft-lb
M_X	rolling moment, ft-lb
M_Z	yawing moment, ft-lb
C_m	pitching-moment coefficient, $M_{Y_S}/qS\bar{c}$
C_l	rolling-moment coefficient, M_X/qSb
C_n	yawing-moment coefficient, M_Z/qSb

$C_{m_{i_t}} = \frac{\partial C_m}{\partial i_t}$ per degree

$C_{l_{\delta a}} = \frac{\partial C_l}{\partial \delta_a}$ per degree

$C_{n_{\delta a}} = \frac{\partial C_n}{\partial \delta_a}$ per degree

$C_{n_{\delta r}} = \frac{\partial C_n}{\partial \delta_r}$ per degree

$C_{l_\beta} = \frac{\partial C_l}{\partial \beta}$ per radian

$C_{n_\beta} = \frac{\partial C_n}{\partial \beta}$ per radian

$C_{Y_\beta} = \frac{\partial C_Y}{\partial \beta}$ per radian

C_L	lift coefficient, F_L/qS
C_D'	drag coefficient, F_D'/qS
C_Y	side-force coefficient, F_Y/qS

$$C_{l_r} = \frac{\partial C_l}{\partial \frac{rb}{2V}}$$

$$C_{n_r} = \frac{\partial C_n}{\partial \frac{rb}{2V}}$$

$$C_{Y_r} = \frac{\partial C_Y}{\partial \frac{rb}{2V}}$$

$$C_{l_p} = \frac{\partial C_l}{\partial \frac{pb}{2V}}$$

$$C_{n_p} = \frac{\partial C_n}{\partial \frac{pb}{2V}}$$

$$C_{Y_p} = \frac{\partial C_Y}{\partial \frac{pb}{2V}}$$

$$C_{l_{\dot{\beta}}} = \frac{\partial C_l}{\partial \frac{\dot{\beta} b}{2V}}$$

$$C_{n_{\dot{\beta}}} = \frac{\partial C_n}{\partial \frac{\dot{\beta} b}{2V}}$$

$$C_{Y_{\dot{\beta}}} = \frac{\partial C_Y}{\partial \frac{\dot{\beta} b}{2V}}$$

$$C_{l_{\dot{r}}} = \frac{\partial C_l}{\partial \frac{\dot{r} b^2}{4V^2}}$$

$$C_{n_{\dot{r}}} = \frac{\partial C_n}{\partial \frac{\dot{r} b^2}{4V^2}}$$

$$C_{Y_{\dot{r}}} = \frac{\partial C_Y}{\partial \frac{\dot{r}b^2}{4V^2}}$$

$$C_{l_{\dot{p}}} = \frac{\partial C_l}{\partial \frac{\dot{p}b^2}{4V^2}}$$

$$C_{n_{\dot{p}}} = \frac{\partial C_n}{\partial \frac{\dot{p}b^2}{4V^2}}$$

$$C_{Y_{\dot{p}}} = \frac{\partial C_Y}{\partial \frac{\dot{p}b^2}{4V^2}}$$

Subscripts:

L,R	left and right control surfaces, respectively
max	maximum amplitude of quantity during an oscillation
s	stability axis

A dot over the term represents the derivative with respect to time; for example, $\dot{\phi} = \frac{d\phi}{dt}$ and $\ddot{\phi} = \frac{d^2\phi}{dt^2}$.

TEST EQUIPMENT

Tunnel

The tests were made in the Langley free-flight tunnel which is housed in a steel sphere 60 feet in diameter and has a 12-foot octagonal test section. This tunnel, which was originally built for flying dynamic models, does not have air-flow characteristics as good as those normally encountered in wind tunnels. The nonuniform airstream-velocity distribution in the region of the test section normally occupied by the force-test model had a negligible effect on the measurements for the static- and the rotary-oscillation-force tests but had a very marked effect on the measurements for the linear-oscillation tests, as will be explained subsequently.

Model

The tests were made by using a model with a sweptback wing and tail typical of current high-speed fighter airplanes. The dimensional characteristics of the model, which was constructed primarily of fiberglass-reinforced plastic and balsa wood, are listed in table I, and a sketch of the model is shown in figure 2. The internal air duct in the fuselage was plugged so that there was no mass flow through the large simulated air inlet. An internal three-component strain-gage balance which measured rolling and yawing moments and side force with respect to the body axis was mounted at the 25.7-percent mean-aerodynamic-chord position.

Apparatus

The static-force tests were made by using the apparatus, shown in figure 3, which permitted the model to be rotated through an angle-of-attack range up to 90° and over an angle-of-sideslip range from -15° to 15°. This apparatus consisted of a curved support strut provided with a track to which the sting was attached by a system of rollers. Angle of attack was determined by the position of the sting along the curved track, and the angle was changed by means of an electric actuator at the base of the sting which engaged with a gearrack on the curved strut. The radius of the track was such that the reference center of gravity of the model was maintained at the same position in the tunnel for all angles of attack. Angle of sideslip was adjusted by rotating the support strut about the vertical axis by using an electric actuator mounted on the base of the support strut.

The rotary-oscillation tests were made by using the apparatus shown in figure 4 and was similar to that described in reference 3. This apparatus consisted of a hollow steel support frame which housed a 5-horsepower variable-frequency electric-motor drive and a cam-operated oscillator unit. The oscillator unit was attached to a horizontal sting so that sinusoidal rotary motion was imparted to the sting as the cam rotated. Maximum amplitude of the sting rotation could be changed by using different cams, but for all tests in the present investigation the maximum amplitude was set at $\pm 10^\circ$. The frequency of the oscillatory motion, which covered a range from 0.5 to 1.0 cycles per second, was varied by changing the frequency of the input electric power. For the rolling tests, the model was mounted with its wings vertical and with the sting coincident with the X body axis as shown in figure 4. For the yawing tests, the model was mounted with the sting coincident with the Z body axis and extending from the bottom of the fuselage as shown in figure 4(b).

The rotary motions generated by this equipment produced lateral displacements, velocities, and accelerations of the model given by the following expressions:

For rolling tests,

$$\left.\begin{aligned}
\phi &= \phi_{max} \sin \omega t \\
\dot{\phi} &= \phi_{max}\, \omega \cos \omega t = p_{max} \cos \omega t \\
\ddot{\phi} &= -\phi_{max}\, \omega^2 \sin \omega t = \dot{p}_{max} \sin \omega t \\
\beta &= \beta_{max} \sin \omega t \approx \phi_{max} \sin \alpha \sin \omega t \\
\dot{\beta} &\approx \phi_{max}\, \omega \sin \alpha \cos \omega t
\end{aligned}\right\} \qquad (1)$$

and for yawing tests,

$$\left.\begin{aligned}
\psi &= \psi_{max} \sin \omega t \\
\dot{\psi} &= \psi_{max}\, \omega \cos \omega t = r_{max} \cos \omega t \\
\ddot{\psi} &= -\psi_{max}\, \omega^2 \sin \omega t = \dot{r}_{max} \sin \omega t \\
\beta &= \beta_{max} \sin \omega t \approx -\psi_{max} \cos \alpha \sin \omega t \\
\dot{\beta} &\approx -\psi_{max}\, \omega \cos \alpha \cos \omega t
\end{aligned}\right\} \qquad (2)$$

Two electrical resolvers which generated alternating-current voltages proportional to the sine and cosine of the angle of shaft rotation were coupled directly to the cam drive shaft so that electrical signals proportional to the angular displacement and velocity of the model were available for use in the readout equipment which will be described subsequently.

The linear-oscillation tests were made by using the apparatus shown in figure 5. The model and strain-gage balance were sting mounted to the "C" frame which was oscillated by a 2-horsepower variable-speed drive motor and flywheel mounted directly above the test section. The frame was supported laterally by ball bearings riding in slotted tubular guide tracks mounted vertically in the floor and ceiling. Rotary motion of the flywheel was transformed to oscillatory motion of the "C" frame by the connecting rod attached to the flywheel and produced a displacement y_{max} of ±0.416 foot. The angle of attack of the model was adjusted by rotating the lower tubular guide track about the vertical axis by using an electric actuator mounted beneath the tunnel floor. The upper guide track was mounted in a sleeve-bearing support and rotated with the frame. A self-alining ball bearing permitted the frame to rotate without twisting the connecting rod.

Two resolvers of the same type as that used with the rotary-oscillation apparatus were geared directly to the flywheel shaft in order to obtain alternating-current voltages proportional to the lateral displacement and velocity of the model.

The motion generated by this equipment produced lateral velocities and accelerations approximated by the following expressions for sideslipping tests:

$$\left.\begin{aligned} y &= y_{max} \sin \omega t \\ \dot{y} &= y_{max} \omega \cos \omega t \approx V\beta_{max} \cos \omega t \\ \ddot{y} &= -y_{max} \omega^2 \sin \omega t \approx -V\dot{\beta}_{max} \sin \omega t \end{aligned}\right\} \tag{3}$$

The velocity and acceleration errors associated with these simplified expressions for the crank-type motion are relatively small, and the effects of these errors on the measured quantities are canceled by use of the special dynamic readout equipment described in the following section.

INSTRUMENTATION AND DATA REDUCTION

The aerodynamic data for both the linear- and rotary-oscillation tests were obtained by using a readout system different from those used in references 3 and 4. This equipment utilized a manually adjusted null system which had the advantage over previous systems of being independent of line voltage, of permitting operation at low frequencies on the order of 1 cycle per second, and of presenting the measured quantities as fixed settings on an indexed dial or counter rather than as fluctuating deflections of a microammeter needle. A block diagram of the system is shown in figure 6, and the inputs to this system and the voltages at the various stages are indicated on the diagram.

A voltage e_{max} of about 10 volts and 3,000 cycles per second produced by the power supply was applied to the sine-cosine resolver being driven at the same angular velocity ω as the model-oscillator unit which produced the motions expressed by equations (1), (2), and (3). The resolver was alined with the model-oscillator units so that the output of the sine winding e_1 was proportional to the displacement of the model, and the output of the cosine winding e_2 was proportional to the linear or angular velocity of the model. At the isolation amplifier either the sine or cosine voltage was selected and passed on to two different circuits. The first circuit consisted of one of the three strain-gage bridge circuits being subjected to an aerodynamic load input L consisting of a component L_1 in phase with the roll, yaw, or sideslip displacement of the model and another component L_2 in phase with the corresponding velocity. The envelope of the output voltage of the strain gage, the product of the aerodynamic load and the displacement or velocity inputs, when $e_1 = e_{max} \sin \omega t$ is used is expressed as

$$e_3 = K_B\left(L_1 \sin^2\omega t + L_2 \cos \omega t \sin \omega t\right) \tag{4}$$

and when $e_2 = e_{max} \cos \omega t$ is used, it is expressed as

$$e_3 = K_B\left(L_1 \sin \omega t \cos \omega t + L_2 \cos^2\omega t\right) \tag{5}$$

where K_B is the strain-gage calibration factor.

The second circuit starting at the isolation amplifier consisted of two manually adjusted attenuators which produced two separate voltages proportional to either e_1 or e_2 as well as to the attenuator settings K_1 and K_2 and of a second resolver, coupled directly to and alined exactly with the first resolver. The input to the resolver consisted of the shaft rotation ω and the two attenuator voltages, one in which e_4 is equal to either $K_1 e_{max} \sin \omega t$ or to $K_1 e_{max} \cos \omega t$ (impressed on the sine winding) and the other in which e_5 is equal to either $K_2 e_{max} \sin \omega t$ or to $K_2 e_{max} \cos \omega t$ (impressed on the cosine winding). The envelope of the resolver output when $e_1 = e_{max} \sin \omega t$ is used is expressed as

$$e_6 = K_R\left(K_1 \sin^2\omega t + K_2 \cos \omega t \sin \omega t\right) \tag{6}$$

and when $e_2 = e_{max} \cos \omega t$ is used, it is expressed as

$$e_6 = K_R\left(K_1 \sin \omega t \cos \omega t + K_2 \cos^2\omega t\right) \tag{7}$$

where K_R is the calibration factor for this part of the circuit.

The voltages e_3 and e_6 were combined, amplified, and read on a sensitive zero-center microammeter. The combined voltage e_7 when $e_1 = e_{max} \sin \omega t$ is used is expressed as

$$e_7 = K_B\left(L_1 \sin^2\omega t + L_2 \sin \omega t \cos \omega t\right) + K_R\left(K_1 \sin^2\omega t + K_2 \sin \omega t \cos \omega t\right) \tag{8}$$

and when $e_2 = e_{max} \cos \omega t$ is used, it is expressed as

$$e_7 = K_B\left(L_1 \sin \omega t \cos \omega t + L_2 \cos^2\omega t\right) + K_R\left(K_1 \sin \omega t \cos \omega t + K_2 \cos^2\omega t\right) \tag{9}$$

This combined voltage e_7 produced a current through the microammeter which caused the needle to deflect proportional to the sum of the voltages in the two circuits. The attenuator settings were adjusted manually to change the values of K_1 and K_2 so that the voltage in the resolver circuit was exactly equal and opposite to the voltage in the strain-gage circuit as indicated by a zero deflection of the needle on the meter. The following relations existed when the system was balanced or nulled:

$$L_1 = \frac{-K_R}{K_B} K_1 = KK_1 \tag{10}$$

and

$$L_2 = \frac{-K_R}{K_B} K_2 = KK_2 \tag{11}$$

where K is the specific overall calibration factor for each of the three strain-gage channels used with the system.

The values of L_1 and L_2 measured for each of the three strain-gage channels and for each of the three types of oscillatory motion were the maximum rolling-moment, yawing-moment, and side-force components produced by the oscillatory motions. These values were reduced to the standard stability-derivative form by using values for the maximum velocity and acceleration components given by equations (1), (2), and (3).

A table of all the stability derivatives measured in these dynamic tests is given as follows:

Derivative	Rolling	Yawing	Sideslipping
In-phase	$C_{l_\beta} \sin \alpha - k^2 C_{l_{\dot{p}}}$ $C_{n_\beta} \sin \alpha - k^2 C_{n_{\dot{p}}}$ $C_{Y_\beta} \sin \alpha - k^2 C_{Y_{\dot{p}}}$	$C_{l_\beta} \cos \alpha + k^2 C_{l_{\dot{r}}}$ $C_{n_\beta} \cos \alpha + k^2 C_{n_{\dot{r}}}$ $C_{Y_\beta} \cos \alpha + k^2 C_{Y_{\dot{r}}}$	C_{l_β} C_{n_β} C_{Y_β}
Out-of-phase	$C_{l_p} + C_{l_{\dot{\beta}}} \sin \alpha$ $C_{n_p} + C_{n_{\dot{\beta}}} \sin \alpha$ $C_{Y_p} + C_{Y_{\dot{\beta}}} \sin \alpha$	$C_{l_r} - C_{l_{\dot{\beta}}} \cos \alpha$ $C_{n_r} - C_{n_{\dot{\beta}}} \cos \alpha$ $C_{Y_r} - C_{Y_{\dot{\beta}}} \cos \alpha$	$C_{l_{\dot{\beta}}}$ $C_{n_{\dot{\beta}}}$ $C_{Y_{\dot{\beta}}}$

TESTS

Static longitudinal force tests were made for an angle-of-attack range from 0° to 90°, for horizontal-tail deflections of 0°, -10°, and -20°, and with the horizontal tail removed. The static lateral force tests were made both with and without the vertical tail for an angle-of-attack range from -10° to 90° and for a range of sideslip angles β from -15° to 15° with all control surfaces at zero deflection. Lateral-control-effectiveness tests were made by using 10° control-deflection increments for each surface. The rotary-oscillation tests were made with amplitudes of roll and yaw of $\pm 10^\circ$, and the linear-sideslipping-oscillation tests were made with an amplitude of the lateral displacement y_{max} of ±0.416 foot. Inasmuch as the sideslip angle was a function of the oscillation frequency as well as of the free-stream velocity and the lateral displacement, the value of β_{max} varied from about $\pm 1.2^\circ$ to $\pm 2.4^\circ$ for these linear-oscillation tests. The frequencies of the oscillations for both rotary and linear tests were 0.50, 0.75, and 1.00 cycles per second which corresponded to values of reduced-frequency parameter k of 0.10, 0.15, and 0.20, respectively. The Reynolds number for these tests was approximately 570,000 based on the mean aerodynamic chord of the model.

Corrections to the out-of-phase derivatives measured in the linear-oscillation tests were required because of the effects of nonuniform airstream-velocity distribution in the wind tunnel on these particular measurements. These effects resulted from the variation of airloads acting on the model as the model traversed the nonuniform airstream in the test section. In order to illustrate how the nonuniform velocity distribution affects the measurements, the two end points of the model's travel during the linear oscillation should be considered. In the case of uniform tunnel air flow, when the model reaches these end points during an oscillation, the model has a zero sideslip angle β, and all the forces and moments acting on the model are attributed to the sideslip acceleration $\dot{\beta}$ which is a maximum. If the tunnel air flow is not uniform, however, there will be some incremental sideslip angle at these end points resulting from the nonuniform air flow and additional forces and moments will be produced which will incorrectly be attributed to the $\dot{\beta}$. Even for very small amounts of flow angularity, these additional forces and moments produced can cause very large errors in the measurements of the sideslipping-acceleration derivatives. In order to account for these errors, tares were applied to the oscillation data based on static-force tests of the model in five different lateral positions in the region of the test section traversed during the oscillation.

PRESENTATION OF DATA

The lift, drag, and pitching-moment characteristics of the complete model as a function of angle of attack are presented in figure 7 for horizontal-tail deflections of 0°, -10°, and -20° and for the horizontal tail removed. Longitudinal- and lateral-control-effectiveness data as a function of α are given in figure 8. The variations of C_l, C_n, and C_Y with β for the different angles of attack are presented in figures 9 and 10 for the vertical-tail-on and vertical-tail-off configurations, respectively. Static lateral stability derivatives based on measurements obtained for $\beta = \pm 2^\circ$ and $\pm 10^\circ$ are summarized in figure 11 for the two configurations tested. The oscillatory lateral stability derivatives for the two configurations for values of k of 0.10, 0.15, and 0.20 are presented in figures 12 to 15 for an angle-of-attack range from -10° to 90°. For sake of clarity in the figures, curves are faired only through the data points for $k = 0.15$.

RESULTS AND DISCUSSION

Static Stability and Control Effectiveness

Longitudinal stability.- The data presented in figure 7 indicate that the complete configuration is longitudinally stable for the complete angle-of-attack range shown and the reference center-of-gravity location. With the horizontal tail off, the wing-fuselage combination is unstable for angles of attack below about 20° but is stable for higher angles of attack.

Horizontal-tail control effectiveness.- The data for $C_{m_{i_t}}$ given in figure 8 are for a mean setting of $i_t = -10^\circ$ and were obtained from the pitching-moment data given in figure 7 for $i_t = 0^\circ$ and -20°. A loss in effectiveness which is attributed to stalling of the horizontal-tail surfaces is shown for angles of attack above 20° although some effectiveness is maintained for all test angles of attack. Changing the mean horizontal-tail setting to trim the configuration to higher angles of attack would delay this loss in effectiveness to higher angles of attack.

L
3
6
5

Rudder-control effectiveness.- A large loss in rudder effectiveness $C_{n_{\delta r}}$ is indicated for angles of attack above about 20° although some amount of effectiveness is maintained over the complete angle-of-attack range. Since this loss in rudder effectiveness occurs at angles of attack where directional divergences and spins are normally encountered, it is evident that the rudder is not suitable as a primary control at angles of attack above 30° or 40°.

Aileron-control effectiveness.- The ailerons lose rolling effectiveness $C_{l_{\delta a}}$ as the angle of attack increases but maintain some effectiveness to above 70°. They also generate relatively large adverse yawing moments at angles of attack above about 30°. Such characteristics usually result in poor lateral control at high angles of attack. A significant fact which perhaps may be overlooked, however, is that the large adverse yawing moments produced by the ailerons at high angles of attack may act favorably during an attempted spin recovery. The recognized procedure for many current airplanes with relatively large values of I_Z/I_X as discussed in reference 5 is to roll the airplane by use of the ailerons in the direction of the spin in order to generate a gyroscopic moment or an inertial interaction to oppose the spinning motion. In this case the aileron yawing moments would oppose the spinning motion directly and assist in effecting the recovery.

Lateral stability.- The variations of the coefficients C_l, C_n, and C_Y with sideslip angle are shown in figures 9 and 10 for the vertical-tail-on and vertical-tail-off configurations, respectively. These data show that the curves for some angles of attack are nonlinear. The plots of C_{l_β}, C_{n_β}, and C_{Y_β} against angle of attack in figure 11, which were based on the data of figures 9 and 10 for sideslip angles of ±2° and ±10°, show some differences in the values of the stability derivatives resulting from this nonlinearity. The values of C_{l_β} based on $\beta = \pm 2^{\circ}$ are larger than those based on $\beta = \pm 10^{\circ}$ over most of the angle-of-attack range. The values of $C_{n_{\beta}}$ based on $\beta = \pm 2^{\circ}$ indicate less directional stability than those based on $\beta = \pm 10^{\circ}$ at the lower angles of attack for the complete configuration. In general, the complete configuration was statically directionally unstable for all angles of attack above about 15° and the vertical tail was ineffective for angles of attack above about 30°. With the vertical tail either on or off, the effective dihedral was positive for the entire angle-of-attack range.

The reduction in the effectiveness of the vertical tail with increasing angle of attack is attributed to air-flow sidewash effects and to a reduction in dynamic pressure at the tail caused by the wing, horizontal-tail, and fuselage wakes which develop as the angle of attack increases. The loss in rudder effectiveness discussed in a previous section illustrates this reduction in dynamic pressure.

Oscillatory Lateral Stability Derivatives

In-phase derivatives.- The variations with angle of attack of the in-phase stability derivatives $\left(\text{which include the stability parameters } C_{l_{\beta}},\ C_{n_{\beta}}, \text{ and } C_{Y_{\beta}}\right)$ for the three types of oscillation tests are shown in figures 12 and 13 for the two configurations and for the three values of k. Included in these figures for comparison are static data $(k = 0)$ obtained from the data presented in figure 11 for $\beta = \pm 10^{\circ}$ which corresponds to the maximum amplitude for the rotary tests.

Comparison of the oscillation data at a given angle of attack for the values of k of 0.10, 0.15, and 0.20 indicates that frequency had only relatively small effects on the derivatives except perhaps in the case of the sideslipping tests. Although some of the spread or scatter in this case may be caused by the effects of differences in sideslip amplitude for the various frequencies, most of the scatter is attributed to the relatively large errors associated with the measurement of very small forces and moments produced by relatively small sideslipping amplitudes. As noted previously, the maximum sideslip amplitude generated by the linear-oscillation equipment operating at the highest frequency is only 2.4°, whereas the maximum amplitude for the rotary tests is 10°. In general, the scatter is less at the lower angles of attack where the air flow around the model was less turbulent and the measurements could be obtained more easily and accurately.

It is doubtful that the rotational acceleration terms, such as $C_{n_{\dot{p}}}$, which are measured in combination with the sideslip terms in the rotary-oscillation tests are significant factors in these measurements inasmuch as the measured values of the combination derivatives were practically independent of frequency. A significant change in the combination derivative $C_{n_\beta} \sin \alpha - k^2 C_{n_{\dot{p}}}$ would have been shown when frequency was changed if the $C_{n_{\dot{p}}}$ derivative were relatively large since its contribution to the combination derivative would have quadrupled as k was increased from 0.10 to 0.20.

Comparison of the static- and oscillatory-test data shows that the curves follow the same general trends and that in most cases the data agree within the experimental accuracies of the tests. In the cases where the curves differ appreciably, the differences may be caused by the effects of frequency in the range between $k = 0$ and 0.10, by the differences in amplitudes of the maximum sideslip angles for the different tests, or by possible support-strut interference tares, all of which were not determined in this investigation because of the additional difficulties involved.

Out-of-phase derivatives.- The variations of the out-of-phase derivatives with angle of attack are given in figures 14 and 15 for the vertical-tail-on and vertical-tail-off configurations, respectively. Included in figure 14 are some unpublished steady-state ($k = 0$) rolling and curved-flow data for C_{l_p} for a similar configuration for comparison with the oscillation data.

The data for the damping-in-roll parameter $C_{l_p} + C_{l_{\dot{\beta}}} \sin \alpha$ given in both figures 14(a) and 15(a) show that damping is maintained over most of the angle-of-attack range but indicate a loss of damping near $\alpha = 20^\circ$ and above $\alpha = 50^\circ$ or 60°. The data show that the vertical-tail contribution to damping in roll is negligible. Comparison of the oscillation data for the different frequencies indicates that there are some effects of frequency at the angles of attack where the damping decreases and that reducing the frequency reduces the damping. Comparison in figure 14(a) of the oscillation data for $C_{l_p} + C_{l_{\dot{\beta}}} \sin \alpha$ with the steady-state rolling-flow data for C_{l_p} shows excellent agreement and suggests that the $C_{l_{\dot{\beta}}} \sin \alpha$ term is negligibly small, at least for angles of attack up to 30°. This does not necessarily mean that $C_{l_{\dot{\beta}}}$ by itself is small since $\sin \alpha$ is small for the low angles of attack.

The oscillation data for the damping-in-yaw parameter $C_{n_r} - C_{n_{\dot{\beta}}} \cos \alpha$ given in figures 14(b) and 15(b) show only relatively small differences in the test points for the different frequencies tested, and the spread in test points appears to be within the experimental accuracy of the measurements. Comparison of the oscillation-test data with some unpublished curved-flow data shows values of C_{n_r} about one-half those for $C_{n_r} - C_{n_{\dot{\beta}}} \cos \alpha$. Part of the difference is attributed to the $C_{n_{\dot{\beta}}}$ term, which is not included in the curved-flow data, as well as to possible effects of frequency for values of k below 0.10. Part of the difference also is attributed to a difference in the nose shapes of the two fuselages. In the unpublished investigation the air inlet at the nose was filled in and rounded, whereas in the present investigation the inlet was open and the internal duct was blocked.

The data for $k = 0.15$ in figure 14(b) are shown in figure 15(b) to indicate the contribution of the vertical tail to the damping in yaw. The contribution of the tail increases with angle of attack for angles of attack up to about 20° and then decreases gradually to about zero as α increases to 50°. This variation is somewhat different from that for the contribution of the tail to static directional stability shown in figure 11, where the contribution is markedly less at $\alpha = 20^{\circ}$ than at $\alpha = 0^{\circ}$ and becomes zero at about $\alpha = 30^{\circ}$. The difference is attributed to the fact that, although sidewash at the vertical tail decreases the tail contribution to directional stability, it increases the contribution to damping because of the time lag involved in the variation of sidewash at the tail.

The data for the derivatives due to sideslip acceleration $C_{l_{\dot{\beta}}}$, $C_{n_{\dot{\beta}}}$, and $C_{Y_{\dot{\beta}}}$ presented in figures 14(c) and 15(c) show a rather large and inconsistent spread in the test points. As previously mentioned the nonuniform velocity distribution in the wind tunnel required the determination of tare corrections which were found to be of the same order of magnitude as the measured quantities. It was, therefore, possible for the net values to have relatively large errors particularly at the higher angles of attack where the model experienced rather severe buffeting due to partial flow separation. These data do not provide sufficiently accurate quantitative values of the various derivatives for use in stability calculations but they do indicate the order of magnitude of the derivatives and the general trend of their variations with angle of attack.

Results of some unpublished tests using the same equipment as that used in the present tests have indicated that measurements of the $\dot{\beta}$ derivatives for some other configurations can be obtained that are more consistent than those obtained in the present tests. In order to obtain consistently accurate measurements of the $\dot{\beta}$ derivatives, however, it appears that the velocity distribution and flow angularity in the region traversed by the model should be much more uniform than those which currently exist in the Langley free-flight tunnel.

SUMMARY OF RESULTS

The results of this investigation to measure the low-subsonic static and oscillatory lateral stability derivatives of a sweptback-wing airplane configuration at angles of attack α from -10° to 90° can be summarized as follows:

1. The complete configuration was longitudinally stable over the entire angle-of-attack range.

2. Both lateral and longitudinal controls lost effectiveness with increasing angle of attack but maintained some amount of effectiveness up to an angle of attack of at least 70°.

3. The complete configuration had positive effective dihedral for all angles of attack tested but was statically directionally unstable for all angles of attack above about 15°.

4. The complete configuration maintained damping in yaw throughout the angle-of-attack range but experienced losses of damping in roll at about $\alpha = 20^{\circ}$ and above $\alpha = 50^{\circ}$.

5. The effects of frequency on the oscillatory lateral stability derivatives were generally small for the range of frequencies tested, but in a few cases the effects were relatively large.

Langley Research Center,
National Aeronautics and Space Administration,
Langley Field, Va., February 26, 1959.

REFERENCES

1. Hewes, Donald E.: Low-Speed Measurement of Static Stability and Damping Derivatives of a 60° Delta-Wing Model for Angles of Attack of 0° to 90°. NACA RM L54G22a, 1954.

2. Boisseau, Peter C.: Low-Subsonic Static Stability and Damping Derivatives at Angles of Attack From 0° to 90° for a Model With a Low-Aspect-Ratio Unswept Wing and Two Different Fuselage Forebodies. NASA MEMO 1-22-59L, 1959.

3. Campbell, John P., Johnson, Joseph L., Jr., and Hewes, Donald E.: Low-Speed Study of the Effect of Frequency on the Stability Derivatives of Wings Oscillating in Yaw With Particular Reference to High Angle-of-Attack Conditions. NACA RM L55H05, 1955.

4. Queijo, M. J., Fletcher, Herman S., Marple, C. G., and Hughes, F. M.: Preliminary Measurements of the Aerodynamic Yawing Derivatives of a Triangular, a Swept, and an Unswept Wing Performing Pure Yawing Oscillations, With a Description of the Instrumentation Employed. NACA RM L55L14, 1956.

5. Neihouse, Anshal I., Klinar, Walter J., and Scher, Stanley H.: Status of Spin Research for Recent Airplane Designs. NACA RM L57F12, 1957.

TABLE I.- DIMENSIONAL CHARACTERISTICS OF MODEL

Wing:	
Airfoil section at root	NACA 65A006
Airfoil section at tip	NACA 65A005
Area (without chord-extension), sq ft	4.63
Span, ft	3.96
Aspect ratio	3.39
Root chord (on fuselage reference line), ft	1.87
Tip chord (without chord-extension), ft	0.462
Tip chord (with chord-extension), ft	0.518
Mean aerodynamic chord, $\bar{c}$, ft	1.309
Sweep of quarter-chord, deg	42
Dihedral, deg	-5
Taper ratio (without chord-extension)	0.247
Horizontal tail:	
Airfoil section at root	NACA 65A006
Airfoil section at tip	NACA 65A004
Area:	
Total, sq ft	1.154
Exposed, sq ft	0.711
Span:	
Total, ft	2.01
Movable panel, ft	0.76
Root chord (on fuselage reference line), ft	1.00
Tip chord, ft	0.148
Sweep of quarter-chord, deg	45
Dihedral, deg	5.42
Aspect ratio (based on total tail area)	3.50
Taper ratio	0.148
Longitudinal distance from 0.257$\bar{c}$ to quarter-chord of tail	1.499
Vertical distance from center of gravity	-0.067
Vertical tail:	
Airfoil section at root	NACA 65A006
Airfoil section at tip	NACA 65A004
Area (dorsal fin exposed and including area of 0.0926 sq ft), sq ft	1.0
Span, ft	1.063
Root chord (on fuselage reference line), ft	1.455
Tip chord, ft	0.380
Sweep of quarter-chord, deg	45
Aspect ratio	1.24
Taper ratio	0.261

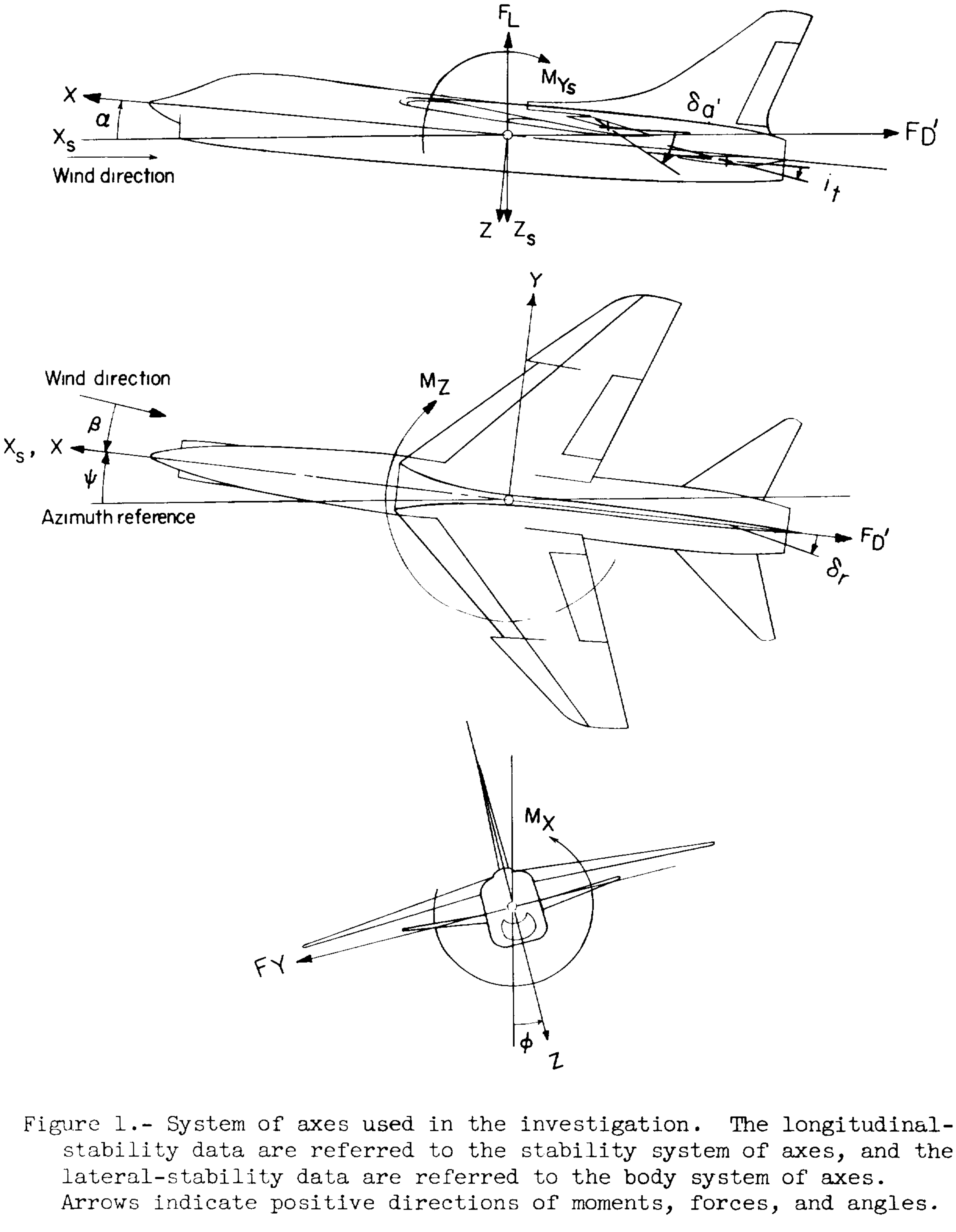

Figure 1.- System of axes used in the investigation. The longitudinal-stability data are referred to the stability system of axes, and the lateral-stability data are referred to the body system of axes. Arrows indicate positive directions of moments, forces, and angles.

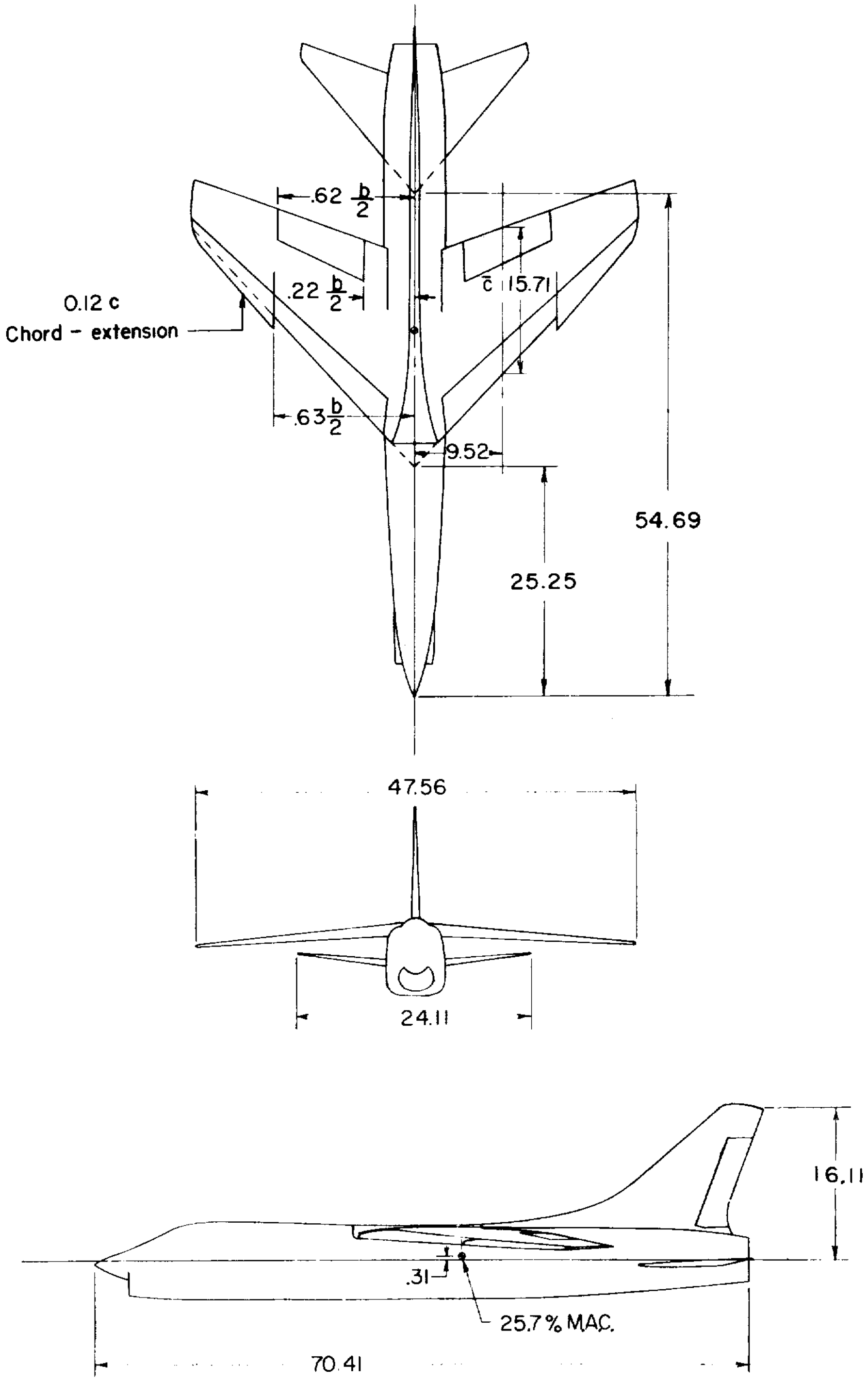

Figure 2.- Three-view drawing of model used in investigation. All dimensions are in inches.

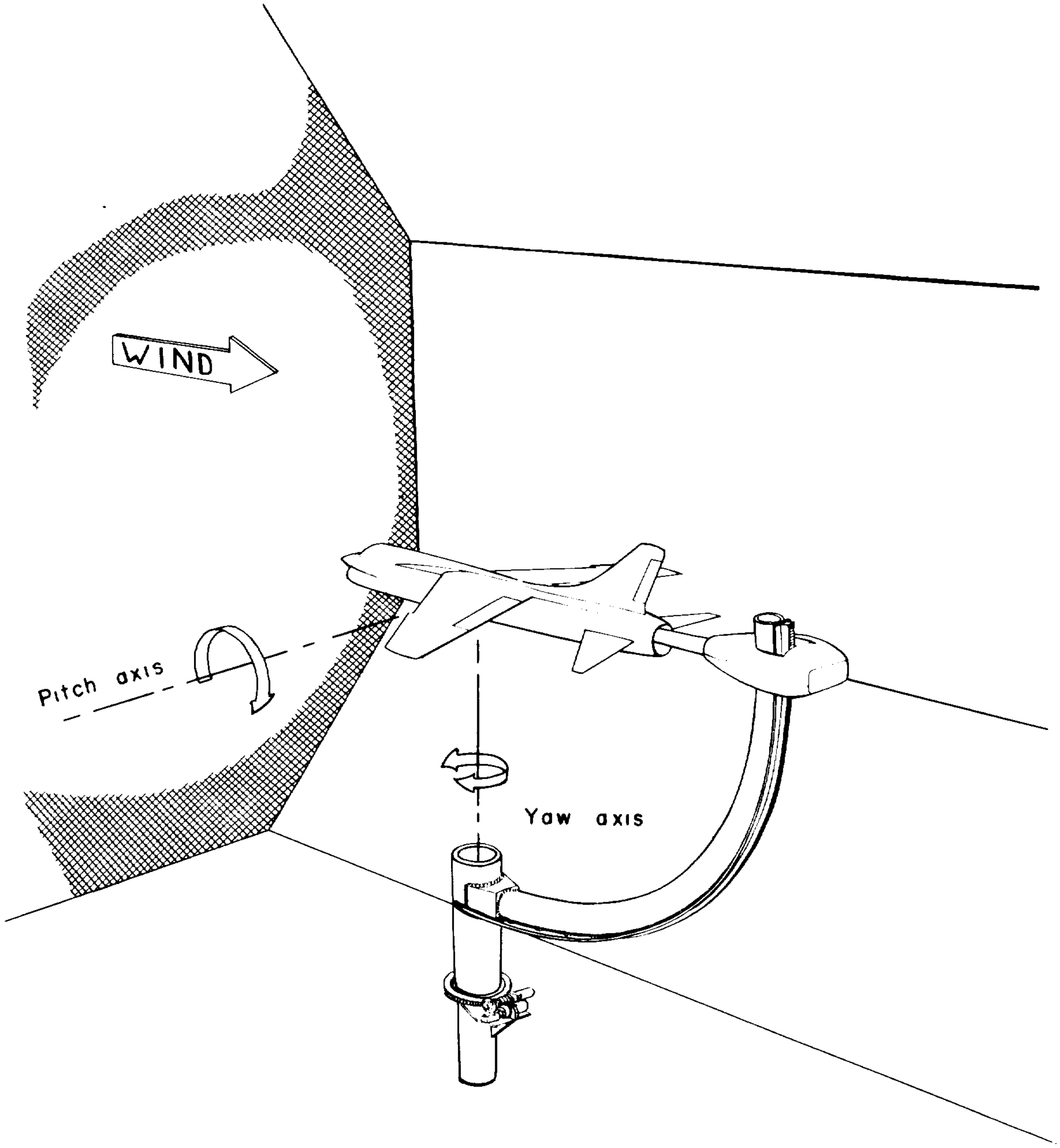

Figure 3.- Schematic diagram of model mounted for static-force tests.

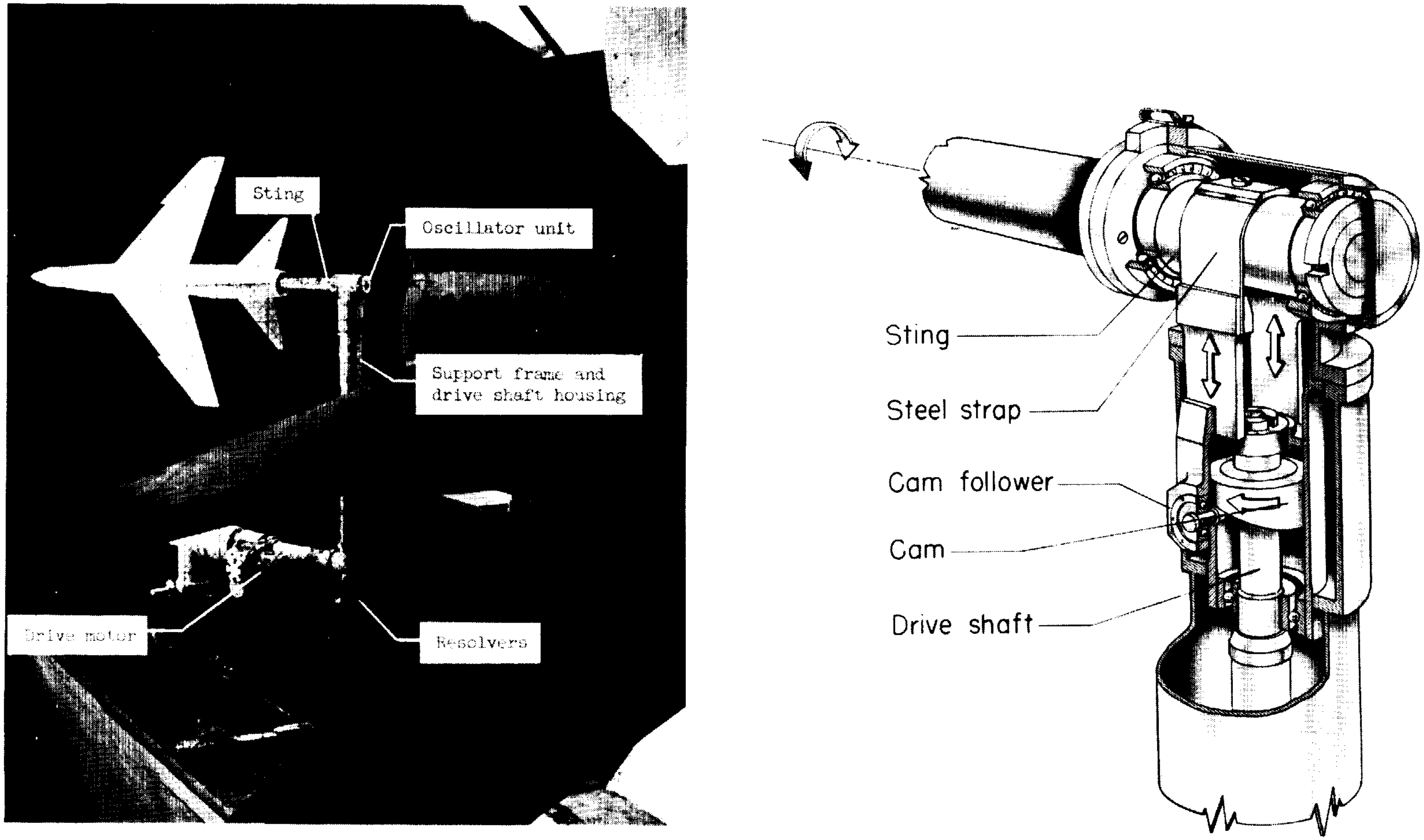

L-58-3490.1

(a) Photograph of model and equipment and sketch of oscillator unit.

Figure 4.- Model installed in the Langley free-flight tunnel on the rotary-oscillation apparatus for rolling tests.

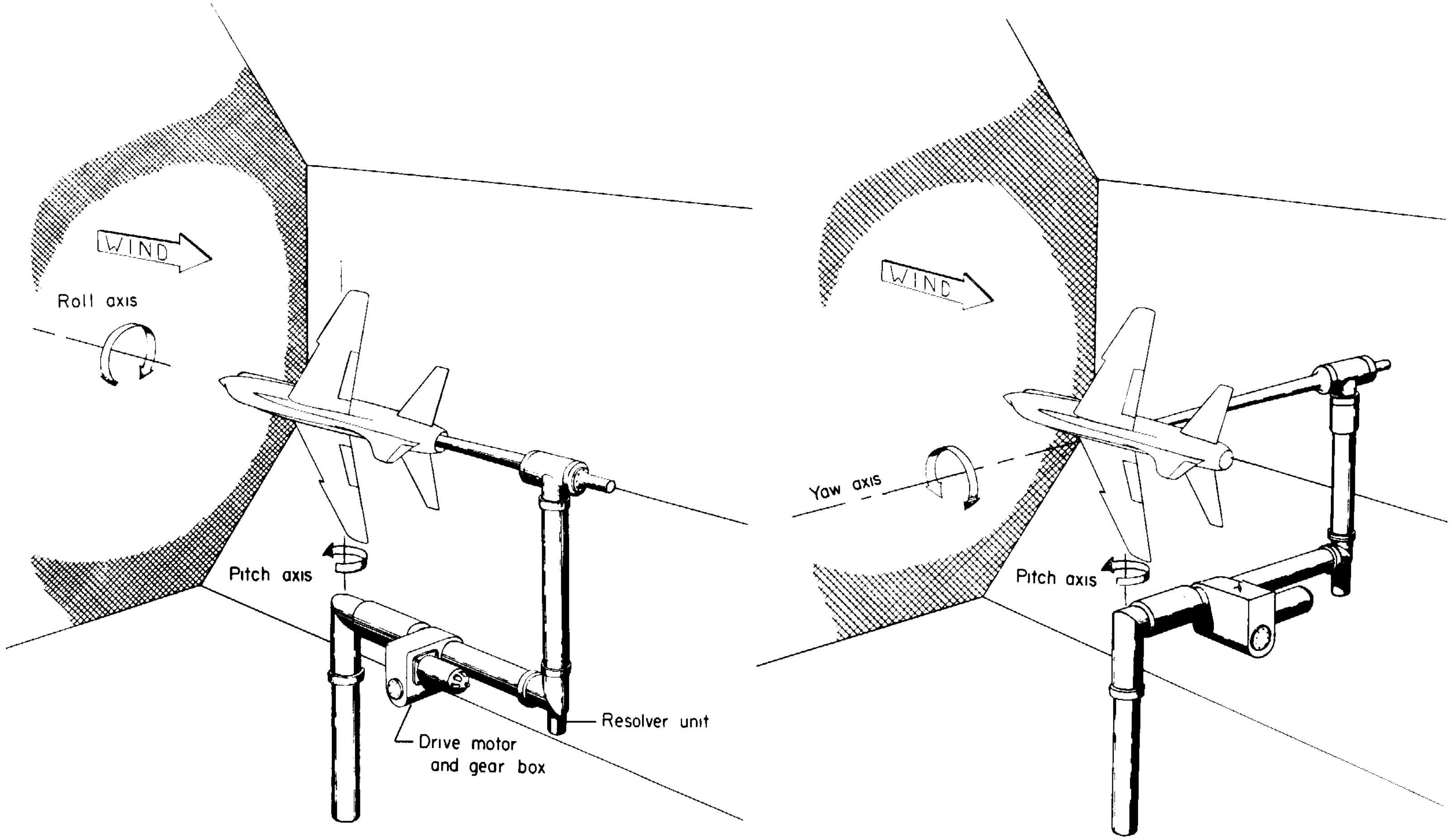

Arrangement for rotary oscillation tests in roll

Arrangement for rotary oscillation tests in yaw

(b) Schematic diagram of model mounted for rotary-oscillation tests.

Figure 4.- Concluded.

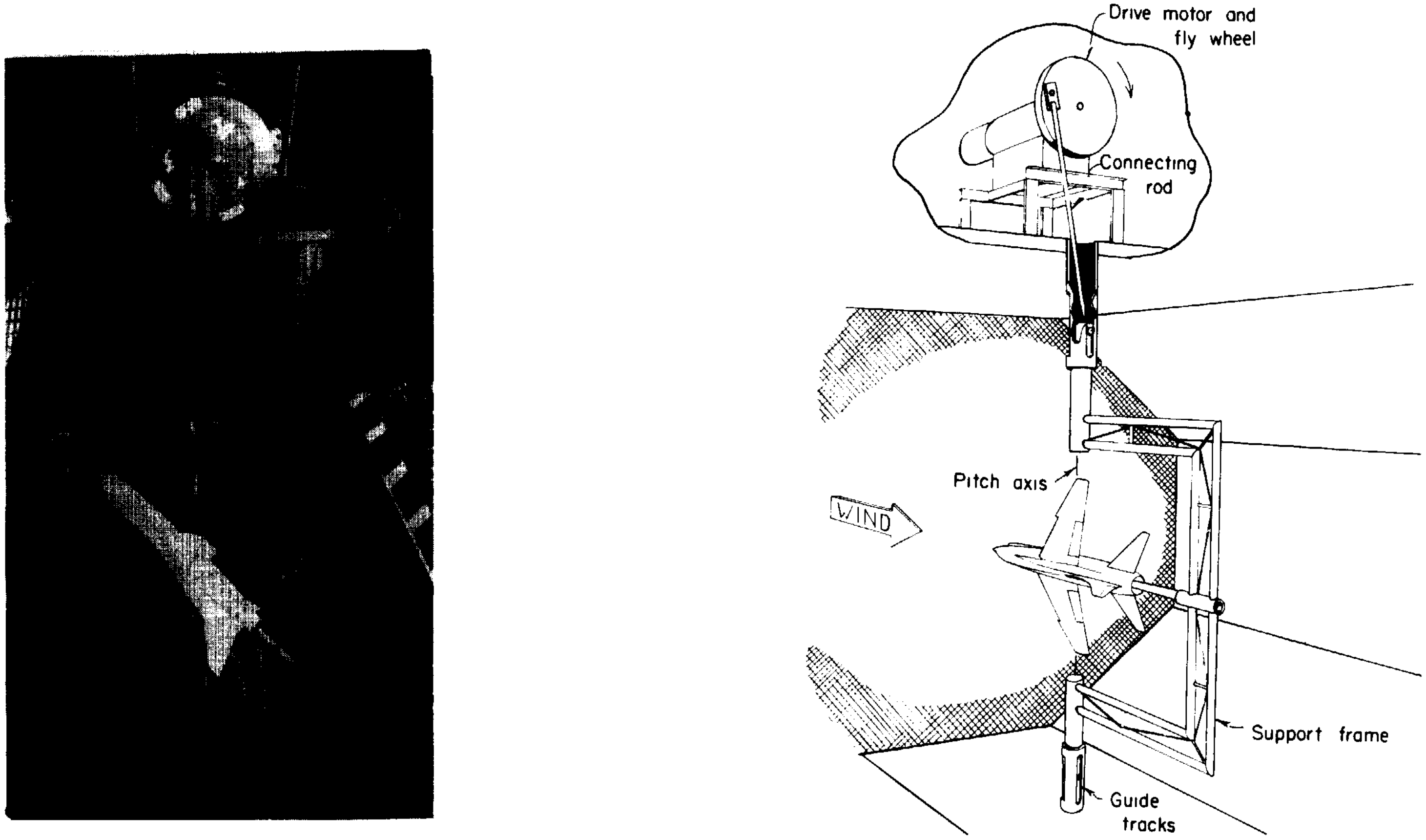

L-58-1304

Figure 5.- Model installed in the Langley free-flight tunnel on the linear-oscillation apparatus for sideslipping tests.

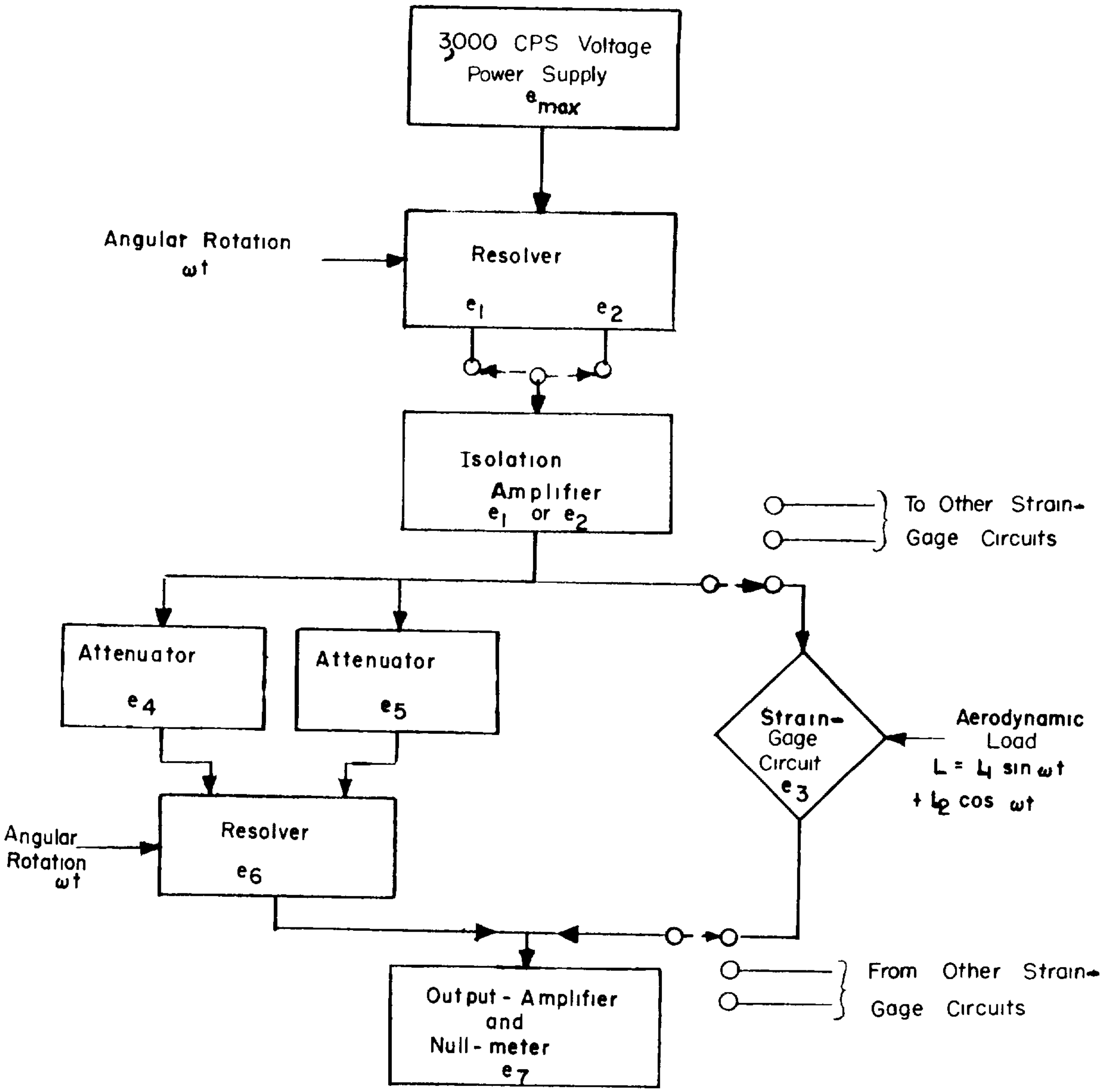

Figure 6.- Block diagram of readout system.

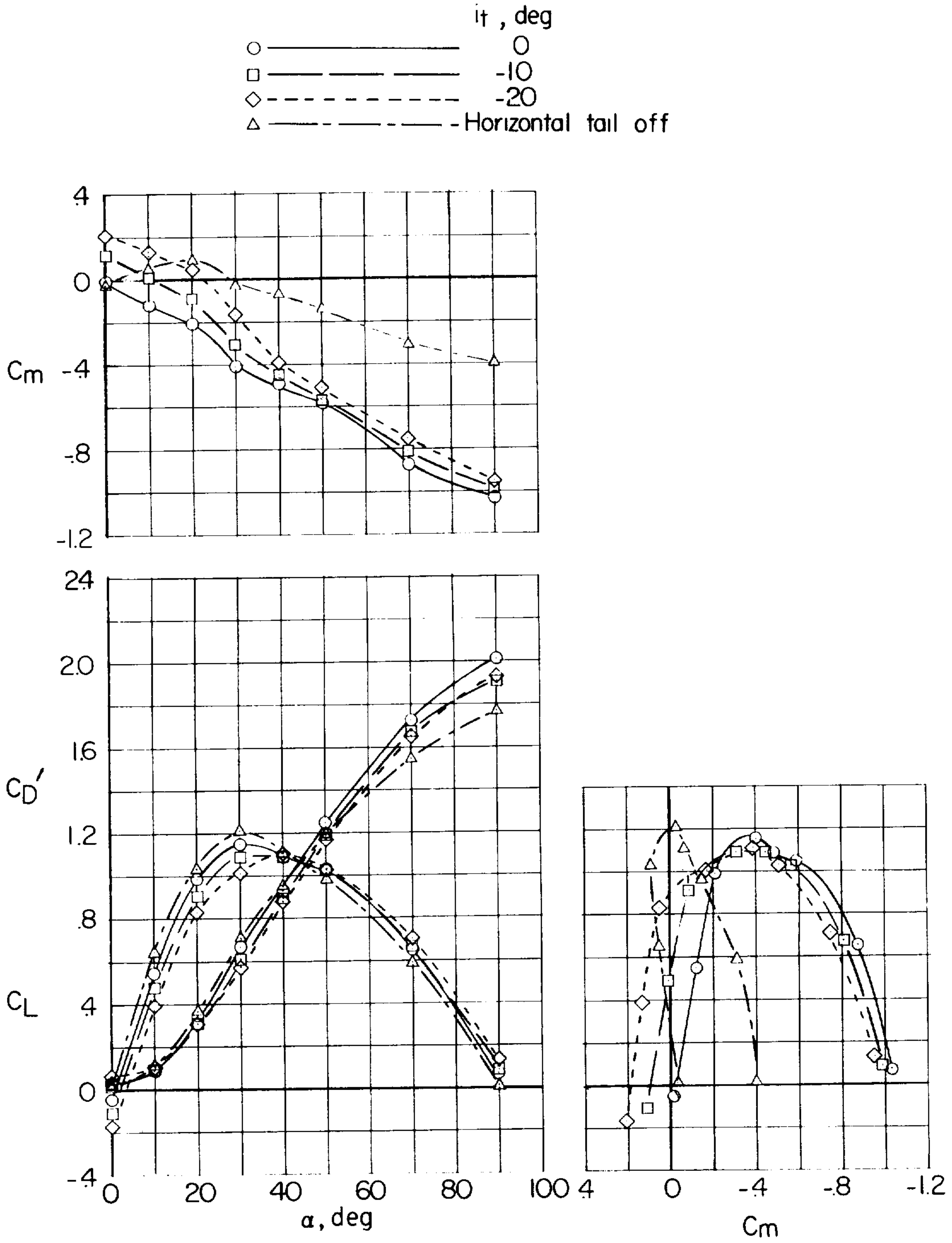

Figure 7.- Variation of static longitudinal stability characteristics with angle of attack. Measurements are referred to the 25.7-percent mean-aerodynamic-chord position.

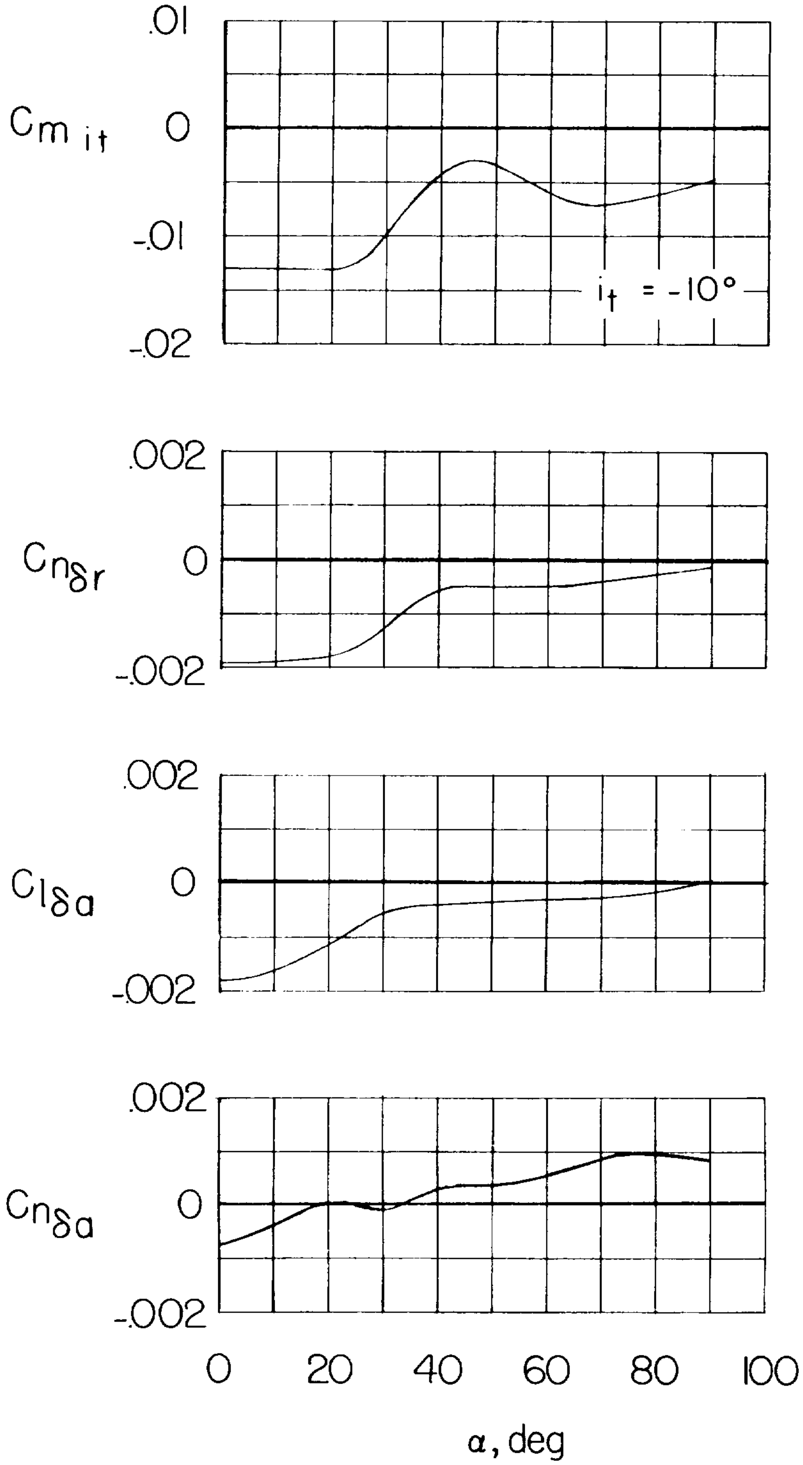

Figure 8.- Variation of control effectiveness with angle of attack.

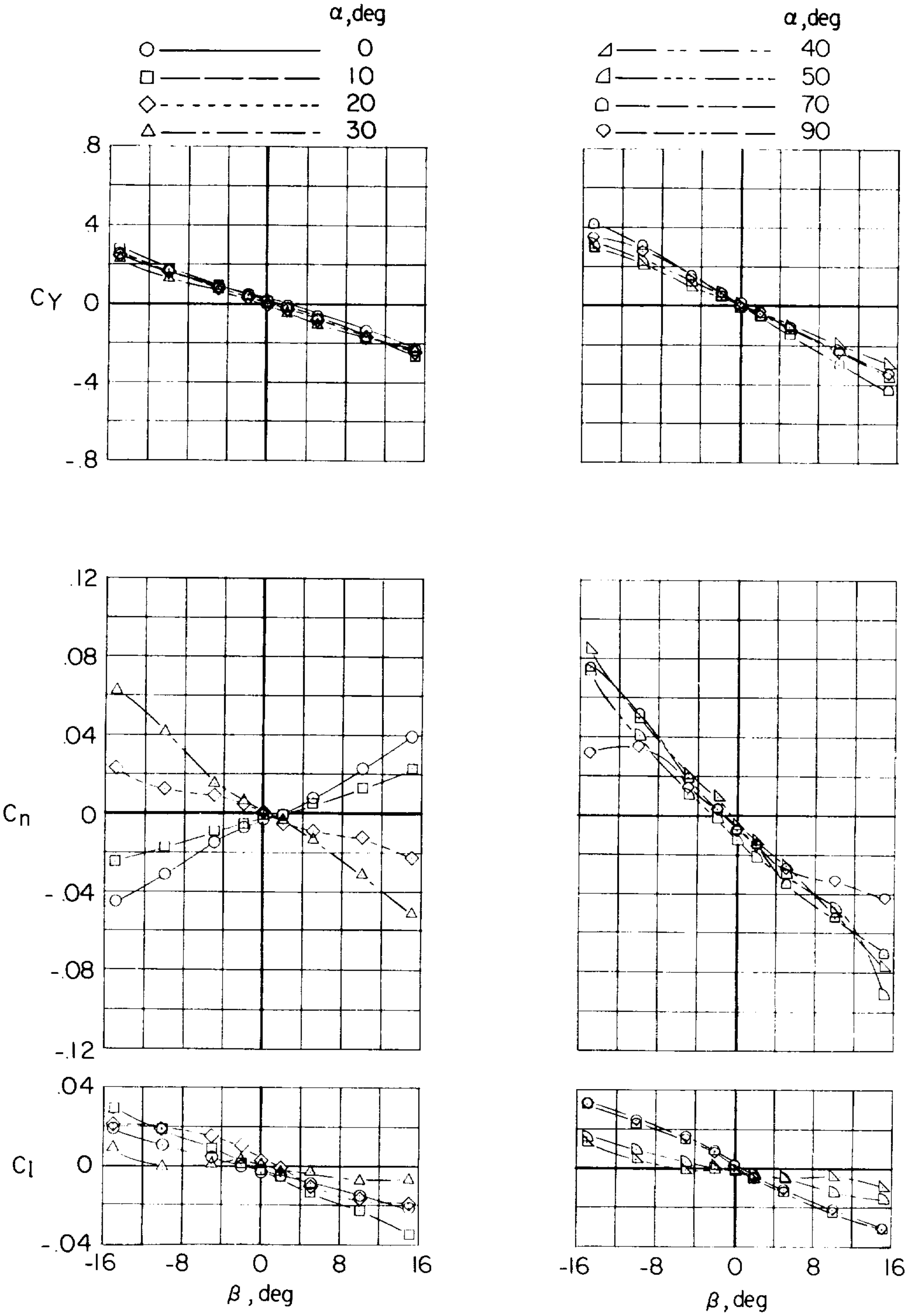

Figure 9.- Variation of lateral forces and moments with angle of sideslip at different angles of attack for the complete model.

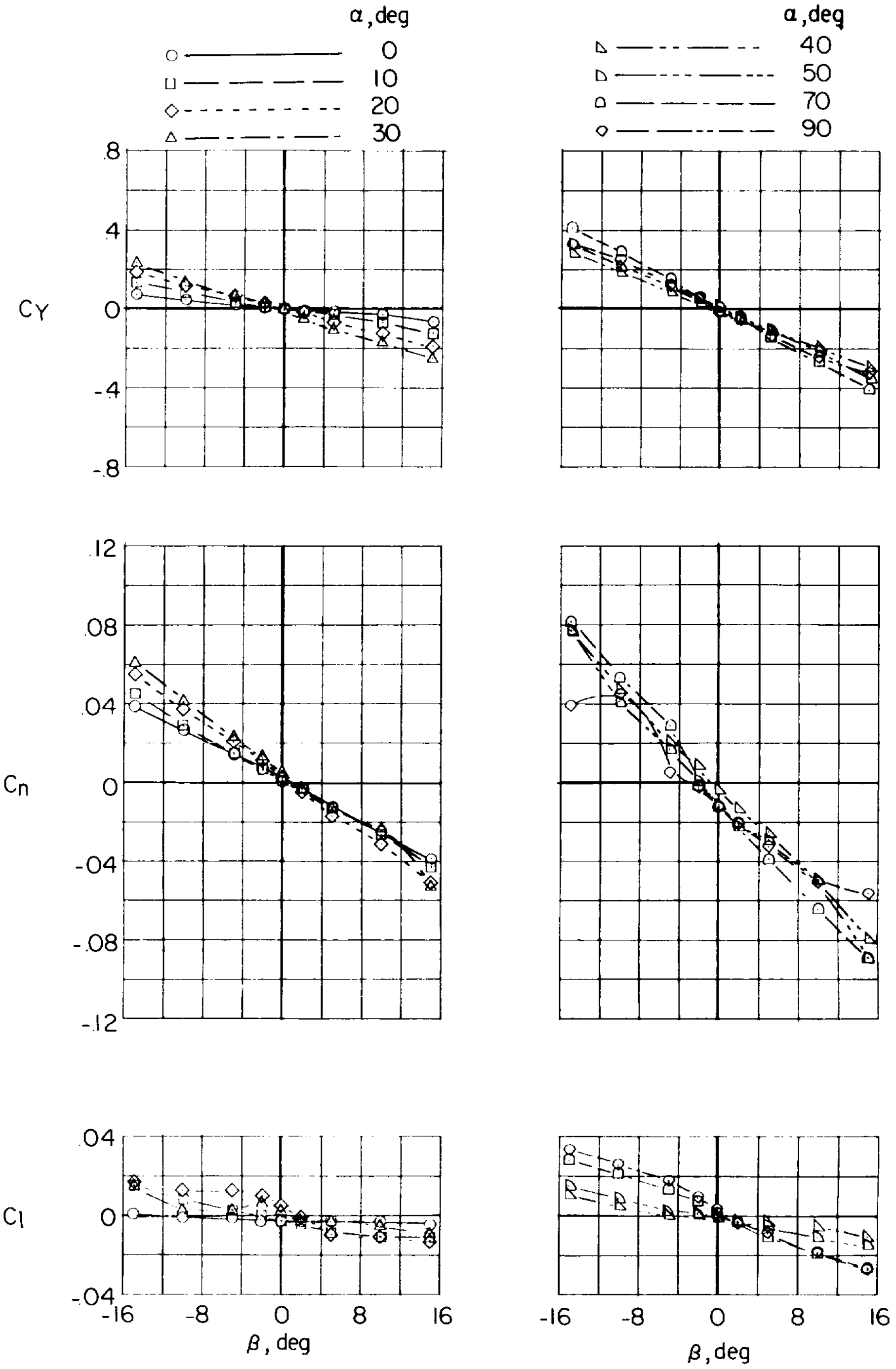

Figure 10.- Variation of lateral forces and moments with angle of sideslip at different angles of attack for the model with the vertical tail off.

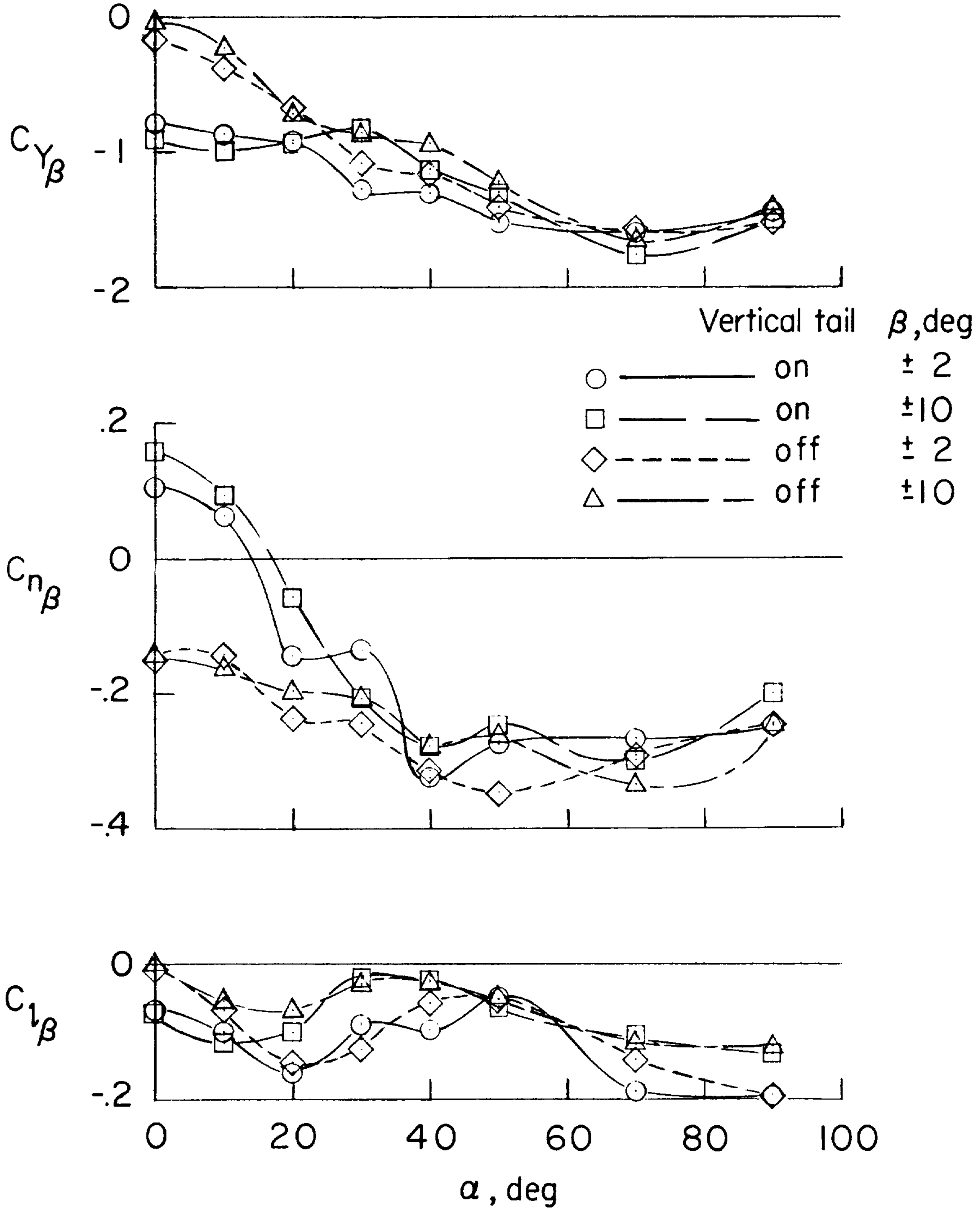

Figure 11.- Variation of static lateral stability characteristics with angle of attack for the test model.

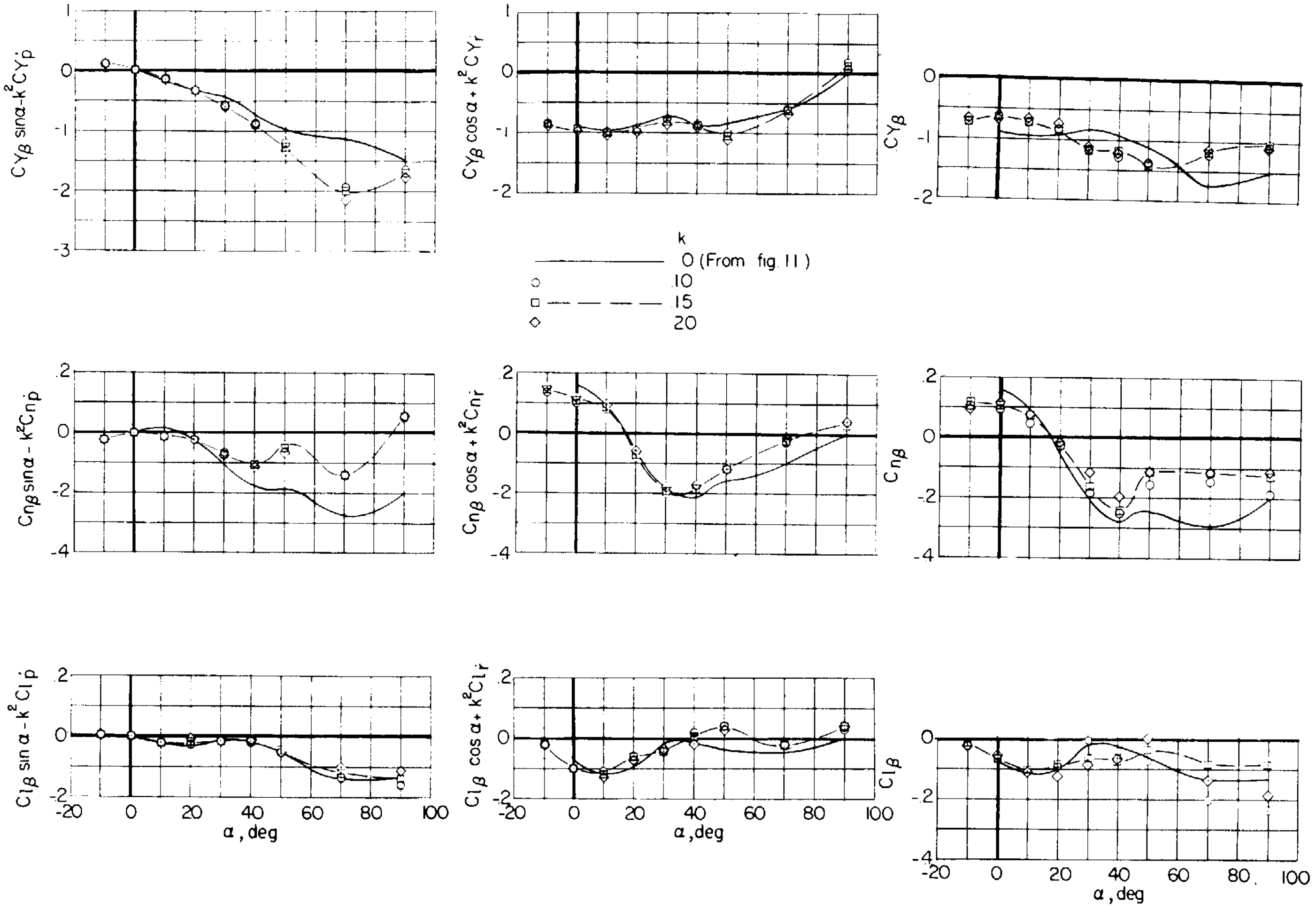

(a) Rolling.

(b) Yawing.

(c) Sideslipping.

Figure 12.- Variation of in-phase derivatives with angle of attack for the complete model at different values of k.

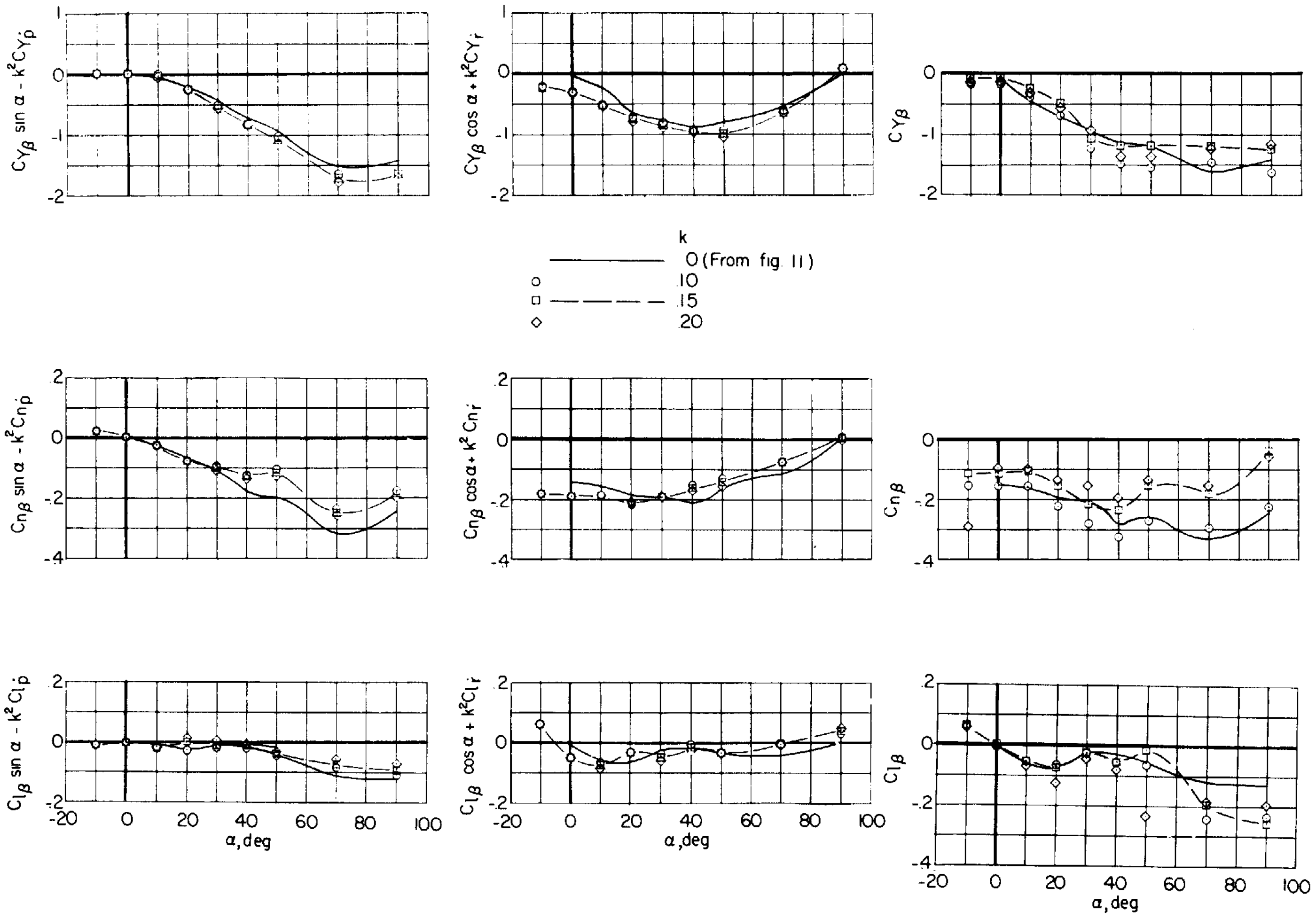

(a) Rolling.

(b) Yawing.

(c) Sideslipping.

Figure 13.- Variation of in-phase derivatives with angle of attack for the model with the vertical tail off at different values of k.

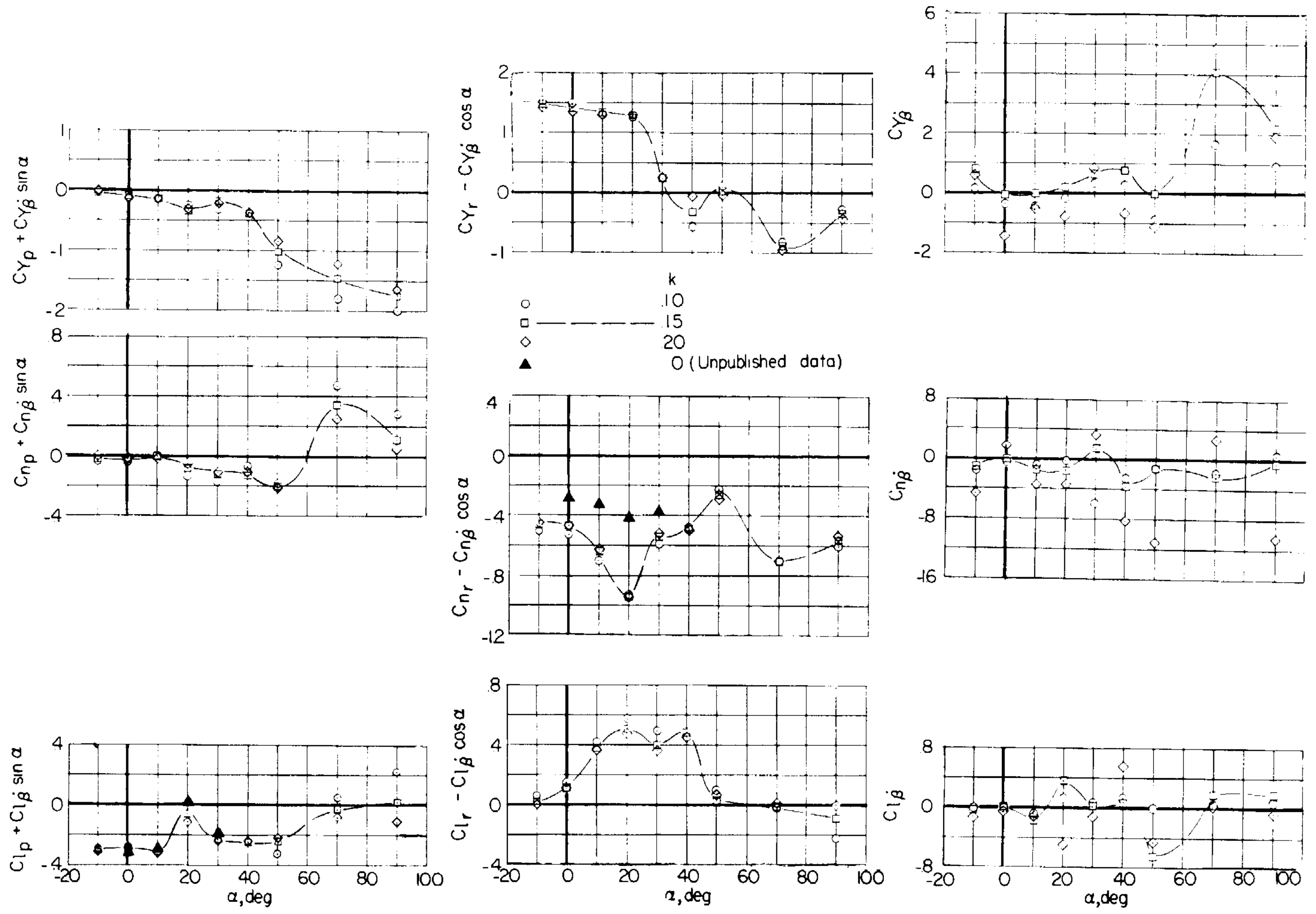

(a) Rolling.

(b) Yawing.

(c) Sideslipping.

Figure 14.- Variation of out-of-phase derivatives with angle of attack for the complete model at different values of k.

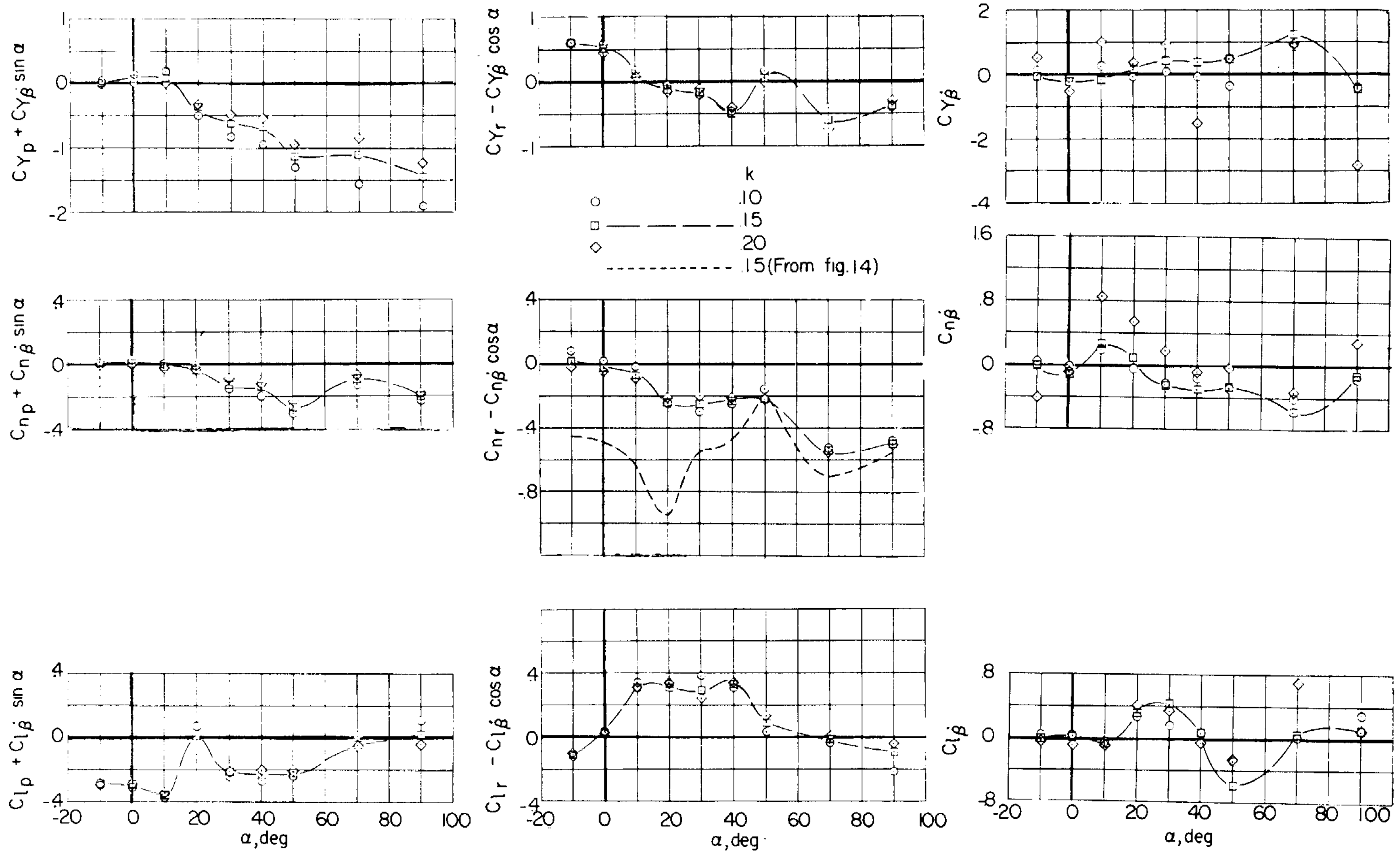

(a) Rolling.

(b) Yawing.

(c) Sideslipping.

Figure 15.- Variation of out-of-phase derivatives with angle of attack for the model with the vertical tail off at different values of k.

NASA MEMO 5-20-59L
National Aeronautics and Space Administration.
LOW-SUBSONIC MEASUREMENTS OF THE STATIC AND OSCILLATORY LATERAL STABILITY DERIVATIVES OF A SWEPTBACK-WING AIRPLANE CONFIGURATION AT ANGLES OF ATTACK FROM -10° TO 90°. Donald E. Hewes. June 1959. 36p. diagrs., photos., tab. (NASA MEMORANDUM 5-20-59L)

The dynamic-force tests consisted of both linear- and rotary-oscillation tests and were conducted at values of the reduced-frequency parameter k of 0.10, 0.15, and 0.20. The configuration was directionally unstable for all angles of attack above about 15° but maintained positive effective dihedral, control effectiveness, and damping in roll and yaw over most of the angle-of-attack range.

Copies obtainable from NASA, Washington

1. Tail-Wing-Fuselage Combinations - Airplanes (1.7.1.1.3)
2. Stability, Static (1.8.1.1)
3. Stability, Lateral and Directional - Dynamic (1.8.1.2.2)
4. Damping Derivatives - Stability (1.8.1.2.3)
5. Control (1.8.2)
6. Research Equipment and Techniques (9)

I. Hewes, Donald E.
II. NASA MEMO 5-20-59L

NASA

NASA MEMO 5-20-59L
National Aeronautics and Space Administration.
LOW-SUBSONIC MEASUREMENTS OF THE STATIC AND OSCILLATORY LATERAL STABILITY DERIVATIVES OF A SWEPTBACK-WING AIRPLANE CONFIGURATION AT ANGLES OF ATTACK FROM -10° TO 90°. Donald E. Hewes. June 1959. 36p. diagrs., photos., tab. (NASA MEMORANDUM 5-20-59L)

The dynamic-force tests consisted of both linear- and rotary-oscillation tests and were conducted at values of the reduced-frequency parameter k of 0.10, 0.15, and 0.20. The configuration was directionally unstable for all angles of attack above about 15° but maintained positive effective dihedral, control effectiveness, and damping in roll and yaw over most of the angle-of-attack range.

Copies obtainable from NASA, Washington

1. Tail-Wing-Fuselage Combinations - Airplanes (1.7.1.1.3)
2. Stability, Static (1.8.1.1)
3. Stability, Lateral and Directional - Dynamic (1.8.1.2.2)
4. Damping Derivatives - Stability (1.8.1.2.3)
5. Control (1.8.2)
6. Research Equipment and Techniques (9)

I. Hewes, Donald E.
II. NASA MEMO 5-20-59L

NASA

NASA MEMO 5-20-59L
National Aeronautics and Space Administration.
LOW-SUBSONIC MEASUREMENTS OF THE STATIC AND OSCILLATORY LATERAL STABILITY DERIVATIVES OF A SWEPTBACK-WING AIRPLANE CONFIGURATION AT ANGLES OF ATTACK FROM -10° TO 90°. Donald E. Hewes. June 1959. 36p. diagrs., photos., tab. (NASA MEMORANDUM 5-20-59L)

The dynamic-force tests consisted of both linear- and rotary-oscillation tests and were conducted at values of the reduced-frequency parameter k of 0.10, 0.15, and 0.20. The configuration was directionally unstable for all angles of attack above about 15° but maintained positive effective dihedral, control effectiveness, and damping in roll and yaw over most of the angle-of-attack range.

Copies obtainable from NASA, Washington

1. Tail-Wing-Fuselage Combinations - Airplanes (1.7.1.1.3)
2. Stability, Static (1.8.1.1)
3. Stability, Lateral and Directional - Dynamic (1.8.1.2.2)
4. Damping Derivatives - Stability (1.8.1.2.3)
5. Control (1.8.2)
6. Research Equipment and Techniques (9)

I. Hewes, Donald E.
II. NASA MEMO 5-20-59L

NASA

NASA MEMO 5-20-59L
National Aeronautics and Space Administration.
LOW-SUBSONIC MEASUREMENTS OF THE STATIC AND OSCILLATORY LATERAL STABILITY DERIVATIVES OF A SWEPTBACK-WING AIRPLANE CONFIGURATION AT ANGLES OF ATTACK FROM -10° TO 90°. Donald E. Hewes. June 1959. 36p. diagrs., photos., tab. (NASA MEMORANDUM 5-20-59L)

The dynamic-force tests consisted of both linear- and rotary-oscillation tests and were conducted at values of the reduced-frequency parameter k of 0.10, 0.15, and 0.20. The configuration was directionally unstable for all angles of attack above about 15° but maintained positive effective dihedral, control effectiveness, and damping in roll and yaw over most of the angle-of-attack range.

Copies obtainable from NASA, Washington

1. Tail-Wing-Fuselage Combinations - Airplanes (1.7.1.1.3)
2. Stability, Static (1.8.1.1)
3. Stability, Lateral and Directional - Dynamic (1.8.1.2.2)
4. Damping Derivatives - Stability (1.8.1.2.3)
5. Control (1.8.2)
6. Research Equipment and Techniques (9)

I. Hewes, Donald E.
II. NASA MEMO 5-20-59L

NASA